Polar stratospheric clouds observed during the Airborne Polar Experiment–Geophysica Aircraft in Antarctica (APE-GAIA) campaign

Francesco Cairo,[1] Alberto Adriani,[1,2] Maurizio Viterbini,[1] Guido Di Donfrancesco,[3] Valentin Mitev,[4] Renaud Matthey,[4] Maurizio Bastiano,[4,5] Gianluca Redaelli,[6] Rossana Dragani,[6] Rossella Ferretti,[6] Vincenzo Rizi,[6] Tiziana Paolucci,[7,8] Livio Bernardini,[7,8] Marco Cacciani,[9] Giandomenico Pace,[5,9] and Giorgio Fiocco[9]

Received 30 June 2003; revised 15 December 2003; accepted 28 January 2004; published 10 April 2004.

[1] In this work, observations of polar stratospheric clouds (PSC) carried out during one flight of the stratospheric research aircraft Geophysica deployed in the Airborne Polar Experiment–Geophysica Aircraft in Antarctica (APE-GAIA) campaign in September–October 1999 are presented. An analysis of data from the two lidars and a backscatter sonde on board the Geophysica aircraft is presented, coupled with temperature measurements. The observations are analyzed with the aid of a mesoscale model to provide air mass thermal histories and a microphysical box model to simulate PSC formation. The results obtained from this comparison are discussed in view of the theories for PSC formation processes. *INDEX TERMS:* 0305 Atmospheric Composition and Structure: Aerosols and particles (0345, 4801); 0320 Atmospheric Composition and Structure: Cloud physics and chemistry; 0340 Atmospheric Composition and Structure: Middle atmosphere—composition and chemistry; *KEYWORDS:* polar stratospheric cloud

Citation: Cairo, F., et al. (2004), Polar stratospheric clouds observed during the Airborne Polar Experiment–Geophysica Aircraft in Antarctica (APE-GAIA) campaign, *J. Geophys. Res.*, *109*, D07204, doi:10.1029/2003JD003930.

1. Introduction

[2] During the polar night, air in the polar stratosphere can radiatively cool to temperatures well below 200 K, thus creating favorable conditions for the formation of clouds [*Stannford and Davis*, 1974]. These polar stratospheric clouds (PSCs) have received great attention in recent years, for the twofold role they may play in the chemistry of the polar stratosphere (see, for review *Solomon* [1999]). Heterogeneous reactions on PSCs' surface can convert chlorine compounds to reactive forms and reactive nitrogen to nitric acid, enhancing chlorine-catalyzed ozone losses. Moreover, large amounts of HNO_3 and H_2O contained in PSC particles may sediment, thus depleting not only the gas phase but also the stratosphere as a whole of water and nitric oxides that otherwise could reform chlorine reservoir species, reducing the active chlorine lifetime.

[3] Chemical reaction rates, as well as denitrification and dehydration potentials, depend on PSCs particles size distribution, composition and thermodynamical state. In the long term, chlorine activation can occur in sufficiently cold conditions irrespective of the type of particles. Nevertheless, it is important to know the exact composition and thermodynamical state of the particles in the cloud in modeling single events. Moreover, the chlorine deactivation and ozone recovery depend on the grade of denitrification and dehydration caused by PSCs, which strongly depends on the PSC's type. Hence the impulse to further study these clouds, their microphysical characteristics and their processes of formation.

[4] An early classification of PSC types [*Poole and McCormick*, 1988a], based on their existence temperatures, grouped them into type 1, forming at temperatures 2–6 K above the frost point T_{ICE}, and type 2, forming below T_{ICE}. Additional lidar investigation of PSC optical characteristics [*Browell et al.*, 1990] led to a further subdivision of PSCs into type 1a, showing low backscattering and high depolarization consistent with few aspherical particles, type 1b, with high backscattering and low depolarization, consistent

[1]Istituto di Scienze dell'Atmosfera e del Clima, Consiglio Nazionale delle Ricerche, Rome, Italy.
[2]Now at Istituto Nazionale per L'Astrofisica-Istituto per la Fisica dello Spazio Interplanetario, Rome, Italy.
[3]Ente per le Nuove Tecnologie, l'Energia, e l'Ambiente Casaccia, Rome, Italy.
[4]Observatoire Cantonal de Neuchâtel, Neuchâtel, Switzerland.
[5]Now at Ente per le Nuove Tecnologie, l'Energia, e l'Ambiente Casaccia, Rome, Italy.
[6]Dipartimento di Fisica, Università degli studi dell'Aquila, L'Aquila, Italy.
[7]Parco Scientifico e Tecnologico d'Abruzzo, L'Aquila, Italy.
[8]Now at Center for the Forecast of Severe Weather by Remote Sensing and Numerical Modelling (CETEMPS), Dipartimento di Fisica, Università degli studi dell'Aquila, L'Aquila, Italy
[9]Dipartimento di Fisica, Università degli studi di Roma "La Sapienza," Rome, Italy.

0148-0227/04/2003JD003930$09.00

with spherical particles that might have been liquid droplets, and type 2, when both backscattering and depolarization attain high values compatible with ice clouds. This classification has now been widely accepted and remains valid even though occasional observations of PSCs not falling into these categories [*di Sarra et al.*, 2002; *Tsias et al.*, 1999; *Tabazadeh and Toon*, 1996] have sometimes led to the suggestion to expand it by introducing new PSC categorizations.

[5] In this work, observations of PSCs performed during the Airborne Polar Experiment–Geophysica Aircraft in Antarctica (APE-GAIA) campaign [*Carli et al.*, 2000] are presented.

[6] The paper is organized as follows: In section 2, a brief description of the microphysical payload on board Geophysica is given. Section 3 describes a flight performed on 2 October 1999, when a strong PSC event was detected. This section contains a survey of the mesoscale meteorological situation that prompted the flight and then describes and discusses the observed PSC characteristics. Section 4 compares the outcomes of a microphysical model to our observations. The possible pathways for PSC formation in light of European Centre for Medium-Range Weather Forecasts (ECMWF) and MM5 model reconstructed air parcel thermal histories are explored. Section 5 is devoted to the conclusions drawn from this study.

2. APE-GAIA Particle Backscatter Payload

[7] The scientific issues that APE-GAIA addressed were mainly the study of the chemistry and transport in the lowermost polar stratosphere in late winter. These goals defined the campaign time period from mid-September to mid-October, normally unfavorable for PSC observations. Nevertheless, PSC climatology from satellite data [*Poole and Pitts*, 1994; *Fromm et al.*, 1997] clearly shows a maximum of PSC occurrence over and eastward of the Antarctic Peninsula. This takes place both because a tropospheric synoptic-scale wave forcing causes a standing structure with the coldest temperatures hovering in that region and because of a more intense lee wave forcing induced by flow over the mountains of the Antarctic Peninsula. In addition, the maximum of the westerly phase of the QBO (which has been shown to enhance PSC occurrence [*Poole et al.*, 1989]) was just occurring within the time frame of the campaign, thus making PSC observations not improbable.

[8] Although the Geophysica scientific payload was not optimized for PSC observations, it hosted three instruments for particle backscatter detection: the long-range lidar Airborne Lidar Experiment (ABLE), the short-range lidar Microjoule Airborne Lidar (MAL), and the in situ backscatter sonde Multiwavelength Aerosol Scatterometer (MAS). Data presented in this paper come from these three instruments. While the measuring range of these instruments is different, they all share the same principle of operation: A monochromatic, polarized, collimated laser light beam is fired into the atmosphere, and the backscattered radiation is collected by a telescope, split into polarized components that are parallel and orthogonal to the polarization of the laser radiation, then detected. These instruments measure essentially the same two parameters, the backscatter ratio and the depolarization ratio. The backscatter ratio may vary from 1 (when no aerosol are present in the sounded air mass) to hundreds for the optically thickest clouds. It can be thought of as a sort of optical mixing ratio, measuring the enhancement of the backscattered light from a portion of the atmosphere when aerosol/cloud particles are present. The depolarization ratio, determined as the calibrated ratio between the noise-corrected orthogonal and parallel signals, measures the change in the state of polarization induced by the scattering process. Air molecules, because of their anisotropic polarizability, induce a slight change in the polarization of the backscattered radiation of the order of a few percent [*Young*, 1980; *Behrendt and Nakamura*, 2002]. Scatterers that are axially symmetric along the direction of the laser propagation induce no depolarization in the backscattering, while asymmetrical scatterers do depolarize. Hence an increase of the depolarized signal occurs in the presence of asymmetrical particles, which we may interpret as solid, while the absence of significant depolarization in the backscattered signal is indicative of spherical particles, which are interpreted as liquid droplets.

2.1. ABLE

[9] The ABLE lidar has been extensively described by *Fiocco et al.* [1999]. It is a long-range 532 nm elastic backscatter lidar capable of pointing at zenith or nadir directions. For this specific flight, the choice of the nadir direction had been done 24 hours before flight. The lidar probed tens of kilometers, starting 1 km from its platform, with a temporal resolution of 60 s and a vertical resolution of 15 m.

[10] Calibration of the signal is obtained comparing the lidar echo to the pure molecular signal in vertical regions where the aerosol contribution can be considered negligible. The molecular signal is calculated from the temperature and pressure vertical profiles obtained by local balloon soundings, when obtainable, from models otherwise. The aerosol contribution is considered negligible at the tropopause level, even if the presence of background aerosol cannot be excluded. During periods of weak volcanic activity the systematic error on the values of the backscattering ratio, arising from this assumption, is less than 0.1. Uncertainties on the retrieval come from the photon-counting statistics and from the procedure for signal calibration and may be assessed to be of the order of 5% for the backscatter and the depolarization ratio.

[11] The vertical coordinate along the flight path is geometric altitude, computed from the flight level as measured by the avionic GPS system. Only data from the first part of the flight are shown since the instrument stopped recording data during the flight, because of a data logger failure.

2.2. MAL

[12] MAL is a package of two lidars, one probing at zenith and the other at nadir. These are upgraded versions of a similar instrument [*Matthey et al.*, 2000] used during the APE-THESEO campaign [*Santacesarea et al.*, 2000]. It employs a miniaturized diode-pumped, frequency-doubled Nd-YAG laser emitting at 532 nm and measures backscatter and depolarization ratio profiles in the vertical direction from 200 m to a few kilometers above and below the aircraft. Backscattering and depolarization profiles are re-

trieved from the backscattered signals by comparing them to those expected from a molecular atmosphere. The molecular profile is retrieved from a model or, where available, from colocated radiosoundings. Calibration of the optical parameters is accomplished by setting the backscatter ratio equal to 1.05 and the depolarization ratio to 1.4%, in regions of atmospheres with minimum aerosol burden: at the tropopause for the downward looking lidar and at the ceiling of the sounding for the upward looking one. The profiles have a vertical resolution of 40 m and are averaged over 60 s, which, given the aircraft speed of 700–750 km/h, leads to a horizontal resolution of 10–15 km. Random uncertainties in the data come from photon-counting statistics and are assessed to be of the order of 5–10% for the backscatter ratio and slightly more for the depolarization ratio. In this paper, the data from the zenith probing lidar are presented. The vertical coordinate along the flight path is geometric altitude, computed from the flight level, as measured by the avionic GPS system.

2.3. MAS

[13] The version of the MAS backscatter sonde deployed in the APE-GAIA campaign differs from the one presented by *Adriani et al.* [1999]. In the current version the backscatter sonde is able to perform backscattering and depolarization measurements in daylight, at 532 nm, and at nighttime at 830 nm as well. It performs measurements of the optical properties of micron-size particles present in the atmosphere in close proximity of the aircraft, ranging from 3 to 30 m from it. The instrument is then adapted to give an in situ characterization of the optical properties of the air masses sampled during the flight. The instrument emits monochromatic linearly polarized beam radiation from low-power laser sources.

[14] Calibration of the signal is accomplished by normalizing the backscattered light to the power emitted by the laser source and comparing this normalized echo to the pure molecular signal that would be expected in regions where the aerosol contribution can be neglected.

[15] The signal that would come from a purely molecular atmosphere is inferred from temperature and pressure measurements acquired along the flight path from the onboard avionic system. The backscatter ratio is posed equal to 1.05 when a region supposed free of any aerosol loading is crossed. This may give rise to systematic errors that might be estimated of the order of 0.05. Other sources of uncertainties on the measurements come from errors in detecting the laser power output, the backscattered light, as well as uncertainties in temperatures and pressures from the avionic readings.

[16] Under average measurement conditions, random errors are of the order of 2% on the 532 nm backscattering ratio, and 5% on the depolarization, in daylight conditions. The data are taken at flight level, the altitude of which is provided by the avionic GPS system. The 10 s temporal resolution of the data allows the resolution of horizontal spatial structures of a few hundred meters.

3. Observations

[17] The particle backscatter payload on board Geophysica detected particles on two occasions: during the flights of 2 and 8 October [*Cairo et al.*, 2000a, 2000b]. The 2 October flight was aimed at investigating a region over the Antarctic Peninsula where strong cooling associated with wave activity was forecasted.

3.1. Meteorological Situation

[18] On 2 October the vortex edge was above the Antarctic Peninsula and almost parallel to it, as depicted in Figure 1, where false color maps of potential vorticity at four isentropic levels from 380 to 450 K potential temperature are shown. The plot is based on the ECMWF-analyzed fields. An intense temperature drop had been observed by PTU sondes launched from the Antarctic Peninsula during the day before. The temperature fall was due to cold air masses advected by southwesterly upper level flow. The MM5 mesoscale model forecasted large temperature oscillations on the lee side of Alexander Island, intensifying above Palmer Peninsula. The PSU/NCAR MM5 is a nonhydrostatic model fully compressible at the primitive equation [*Ferretti et al.*, 2000] and has been extensively used to forecast lower stratospheric waves during APE-GAIA (R. Ferretti et al., manuscript in preparation, 2003). The model configuration allows the modeling of wet processes, and a simple planetary boundary layer parameterization is used. The domain is centered at 60°S, 65°W. A two-way nesting technique is used for enhancing wave phenomena over a defined area, such as the Antarctica Peninsula. The coarse domain covers the area from 68°S, 90°W to 51°S, 60°W with a grid size of 36 km, whereas the innermost domain (67°S–75°W, 62°S–57°W) has a grid size of 12 km. A terrain following coordinate is used with 52 vertical levels unequally spaced, increasing resolution upward for both domains. The top of the model is at 30 hPa. The ECMWF data analyses at 0.5 degree resolution, upgraded every 6 hours, are used to initialize the model.

[19] On the basis of the 36 hour MM5-forecasted scenario, a flight plan was designed and specifically aimed to lead toward the regions where the background low-temperature field and the intense orographic wave activity were forecasted. Both conditions were fulfilled on 2 October 1999.

3.2. Flight Path

[20] The plane took off from Ushuaia at approximately 0500 UTC. After a fast climb to the altitude of 17 km, the airplane carried out the first leg of a triangular route with a stepwise altitude profile at 17, 17.5, 18 and 18.5 km heading southward on a constant longitude pathway.

[21] After approximately 2 hours of flight, over the sea ice limit, the pilot reported an observation of stripes of clouds below the aircraft, starting to be illuminated by the rising Sun. Approaching the southernmost point of the flight path at 0700 UTC the temperature started to drop drastically, and moderate turbulence set in. Turbulence became stronger on the second leg of the flight heading northeast across the Antarctic Peninsula, when the pilot reported the presence of clouds along and above the flight level. This second leg was a quasi-Lagrangian one since the aircraft flew parallel to the air flux streamlines.

[22] After the easternmost point of the peninsula was reached, the aircraft turned in the direction of Ushuaia on the third leg of the flight path. The temperature increased, and the turbulence disappeared. During this third leg the

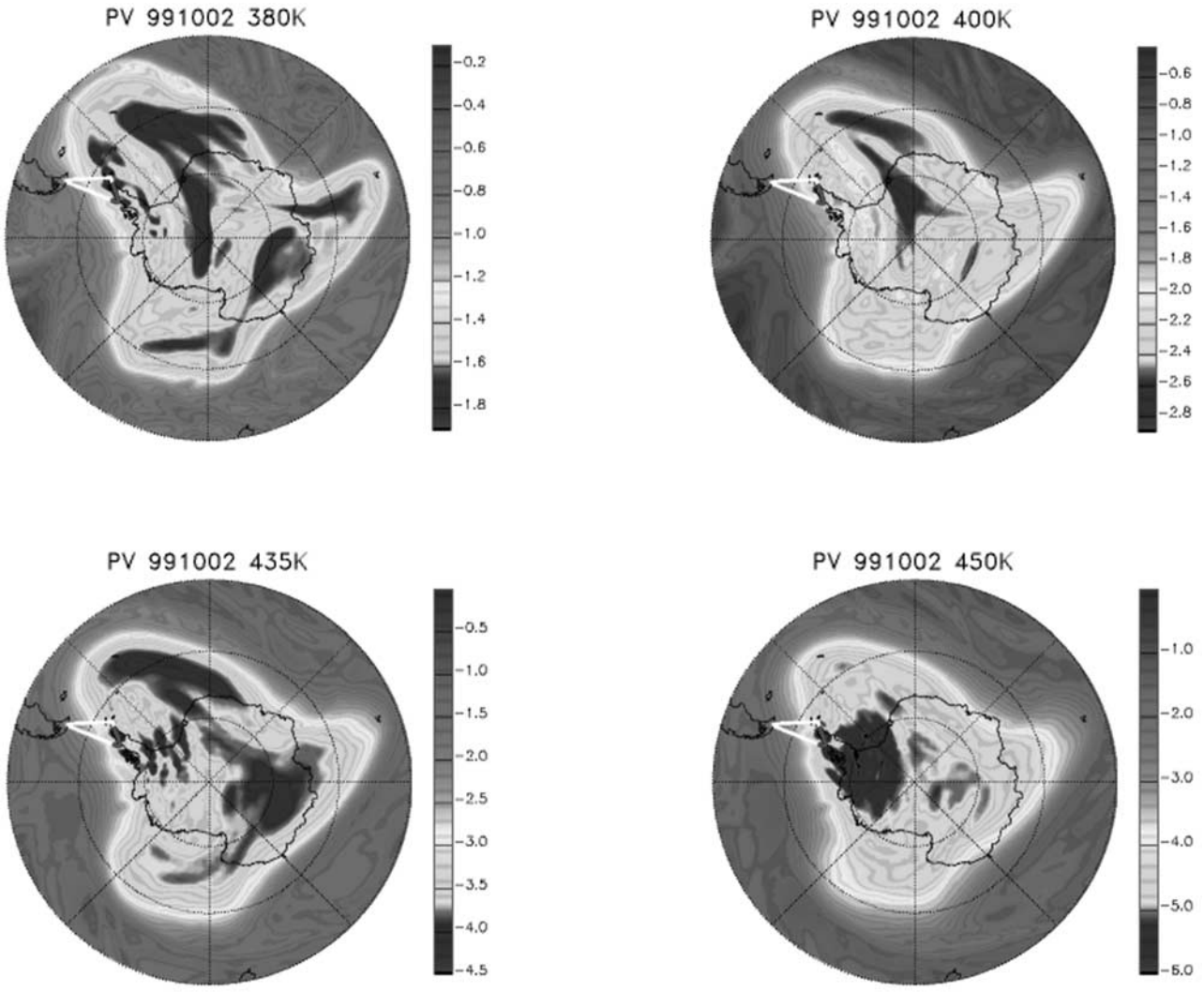

Figure 1. False color image of isentropic potential vorticity at 380, 400, 435 and 450 K isentropic levels, for 2 October at 0600 UTC, based on the ECMWF-analyzed fields. The outer edge of the polar vortex corresponds roughly to the yellow-colored region. The white solid line shows the flight trajectory. Regions along the flight where PSC observations took place are evidenced in red. See color version of this figure in the HTML.

aircraft climbed to the altitude of 19 and then 20 km. The aircraft landed in Ushuaia at approximately 1045 UTC.

[23] In Figure 1 the flight trajectory is also shown as a white solid line. The segments of the flight where PSCs have been observed are evidenced in red. These PSC observations took place during the whole second leg of the flight, which extended for more than 600 km parallel to the vortex edge, along the Antarctic Peninsula.

3.3. Cloud Observations

[24] A time series of the MM5-forecasted temperature field along part of the aircraft flight path is shown in Figure 2. Two large temperature oscillations are discernible. These are in good coincidence with the presence of enhanced backscatter ratio observed by lidars and backscatter sonde, which in the graph are superimposed on the temperature field and color-coded. The success of the flight in observing PSCs where their presence was predicted is demonstrated by the good agreement between the locations of the forecasted temperature oscillations and the towering clouds detected by MAL above the aircraft.

[25] Figures 3 and 4 show the backscattering and depolarization ratio, respectively, observed by the instruments during the first leg of the flight from Ushuaia to the southernmost point of the flight versus latitude.

[26] ABLE detected a continuous thin deck of low-level, optically thick fog, or stratus-like clouds (mark 1 in Figures 3 and 4) extending all the way down to Antarctica. The top of these structures was found at an altitude of a few hundred meters above sea level, with a marked discontinuity in altitude at 61°S, roughly corresponding to the limit of sea ice. These low-level clouds, despite their low geometrical thickness, were optically so thick as to attenuate completely the ground return signal. For that reason, it was not possible to observe the lower edge of those clouds, which might as well extend down to sea level. Their strong depolarization,

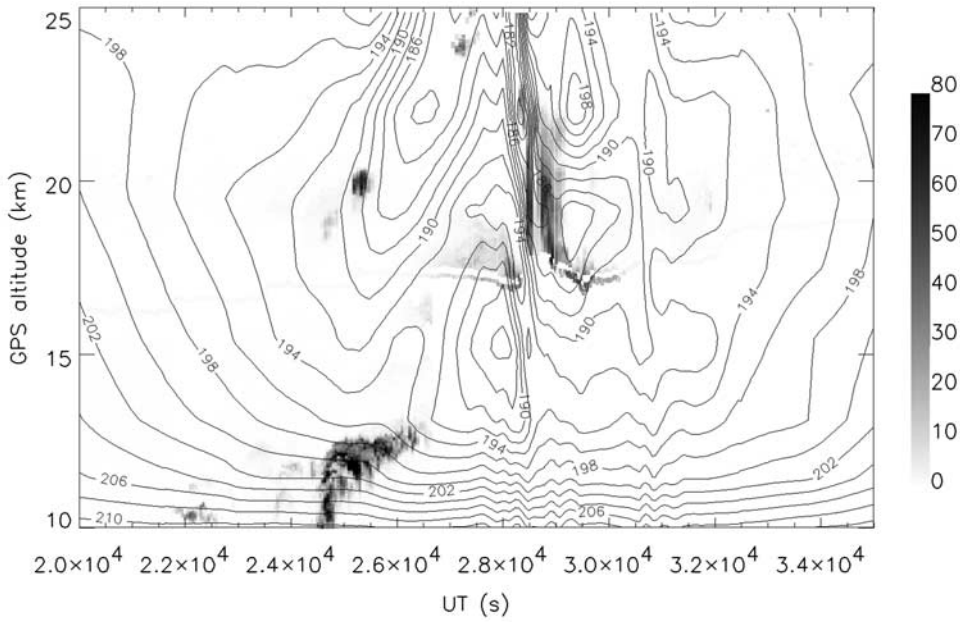

Figure 2. Time series of the vertical sections of the MM5-forecasted temperature field along the flight path. The backscattering ratio observed by lidars and backscatter sonde are superimposed and color-coded. The agreement between temperature oscillations and the clouds detected shows the success of the flight in observing PSCs where their presence was actually predicted by the mesoscale model. See color version of this figure in the HTML.

which increased going northward, could as well be attributed to multiple scattering rather than to ice crystals. Other structures of high tropospheric cirrus clouds were detected in the altitude range from 10 km to 13 km between 60°S and 66°S (mark 2). The layered structure of these clouds, with very high backscattering and medium to high depolarization, extended into the stratosphere as the aircraft flew southward. The tropopause was situated at 13 km, as measured by a PTU sounding launched on the same day from Rothera (67.6°S, 68.1°W). Those clouds seemed already to be associated with the wave activity going on in the area. Getting closer to the Antarctic land, patches of PSCs were also detected at altitudes of 19 km (mark 3) and 25 km (mark 4). These were in the stratosphere and

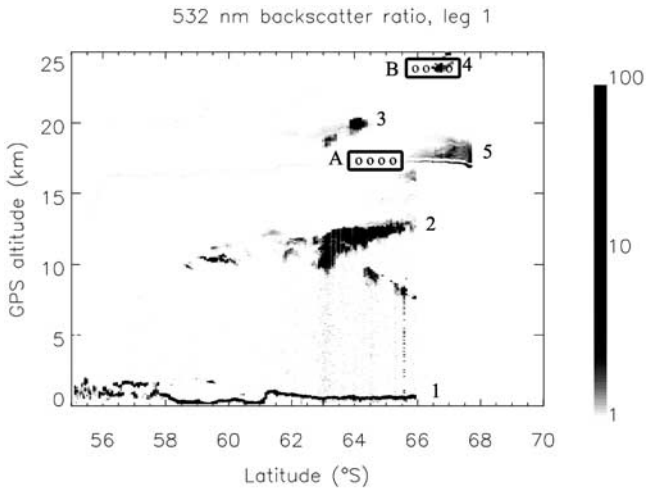

Figure 3. Color-coded backscatter ratio versus altitude-latitude, as observed by the instruments along the first leg of the flight. Polar stratospheric clouds started to appear at 62°S as patchy structures above the aircraft flight level. On approaching the Antarctic Peninsula, a large area of PSC was observed above and below the aircraft level. Two regions of interest (ROI) framed in boxes have been chosen for detailed backward temperature history studies. The backtrajectories' starting points are marked with open circles. See color version of this figure in the HTML.

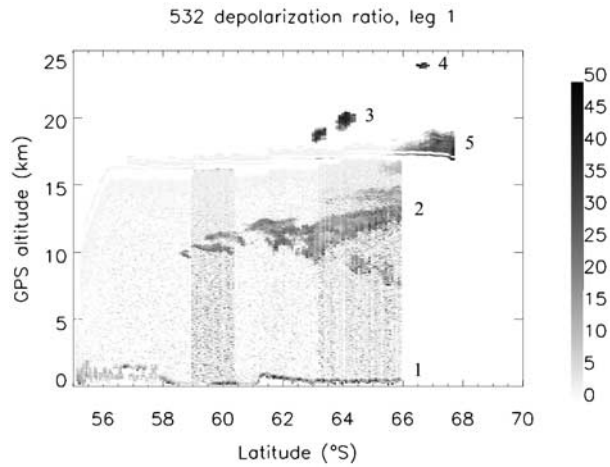

Figure 4. Color-coded depolarization ratio versus altitude-latitude. The high values of depolarization of all the clouds encountered above, at and below the flight level are indicators of the presence of solid particles in the clouds. See color version of this figure in the HTML.

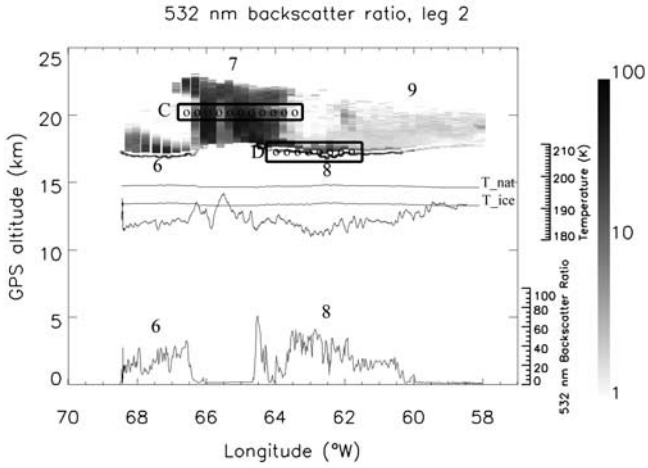

Figure 5. In the upper part, color-coded backscatter ratio observed during the second leg of the flight. Two regions of interest (ROI C and ROI D) framed in boxes have been chosen for detailed backward temperature history studies. The backtrajectories' starting points are marked with open circles. In the middle part of the figure, air temperature recorded during the flight by the aircraft sensors, superimposed on T_{NAT} and T_{ICE} computed assuming 10 ppbv of nitric acid and 5 ppmv of water vapor. In the lower part, backscatter ratio detected in situ by the backscatter sonde. These latter two plots show good coincidence between low temperatures and high backscatter ratios. See color version of this figure in the HTML.

probably in air outside the vortex area. Close to the southernmost point of the flight path, a large PSC extending from 15 km to 19 km (mark 5) started to be revealed by the lidars and backscatter sonde. The oscillating, wavy structure of this cloud, following the air streamlines, could be discerned in the first part of the cloud, below flight level, detected by ABLE with high time resolution. Analysis of depolarization data shows how these clouds are highly depolarizing, thus predominantly composed of solid particles.

[27] Figure 5 shows the color-coded backscatter ratio observed during the second leg. It also shows the temperature recorded during flight by the aircraft sensors, superimposed on T_{NAT} [*Hanson and Mauersberger*, 1988] and T_{ICE} [*Marti and Mauersberger*, 1993], computed assuming 10 ppbv of nitric acid and 5 ppmv of water vapor.

[28] The high backscattering ratio detected in situ by MAS is reported in the lower part of the figure: It appears well coincident with the low temperatures recorded along the flight path.

[29] Figure 6 shows, in color-coding, the depolarization ratio measured by MAL and MAS. The latter is also reported for clarity in the lowermost part of the figure. Noteworthy is the observation of two towering type II PSCs (mark 7) extending from 17 km up to 23 km, with backscattering ratios as high as 60–70 and depolarizations around 30–35%. These towering ice PSCs are embedded in an area of moderate backscatter ratio and strong depolarization. Unfortunately, there is a lack of MAS data in a 6 min window coincident with the base of this two-tower pattern. However, from the backscatter values recorded at the edge of this window it does not seem that these ice towers extended down to the aircraft level. An area of PSC, marked 6 in the figures, precedes the towers and extends slightly less in the vertical. These have also been observed by MAS at the aircraft altitude. While at the aircraft altitude the backscatter and depolarizations are consistent with a type II PSC, at higher levels the decreased backscatter ratio suggests a type Ia PSC. After and downwind of the two-tower pattern, there is a large area of enhanced backscatter and depolarization ratio, starting at the flight level (mark 8) and extending upward to 20 km (mark 9). At the aircraft level, the characteristics of the cloud match well with a type II PSC, while higher up there is a vast area where the volume depolarization ratio at 10% and the lower values of the backscatter ratio are more consistent with a type Ia PSC.

[30] The PSC optical characteristics are consistent with a type II PSC for most of the observations, albeit in some areas the data suggest the presence of type Ia PSC; aerosol depolarization ranges from 10% to 40% throughout the observed cloud.

[31] Noteworthy, in these observations, is the complete absence, to any significant extent, of portions of the clouds where the particles could be considered as liquid. This contrasts with similar observations of wave-induced PSCs in the Arctic where liquid type Ib PSCs always seem to develop in similar conditions [*Dörnbrack et al.*, 2002; *Voigt et al.*, 2000a].

[32] The air temperature recorded along the second leg of the flight path, between 65°W and 60°W, allowed us to compute the corresponding water vapor saturation pressure with respect to ice. Aerosol backscattering coefficient has been computed from the backscatter ratio measured by MAS. The scatterplot of these two quantities is depicted in Figure 7: Although scattered, the plot clearly shows a correlation between aerosol backscattering coefficient and water vapor saturation pressure. Very rapid heating/cooling in wave events may lead to condensed substances out of thermodynamical equilibrium with their vapor phase. Nevertheless, the fast response of water vapor/ice to changes in

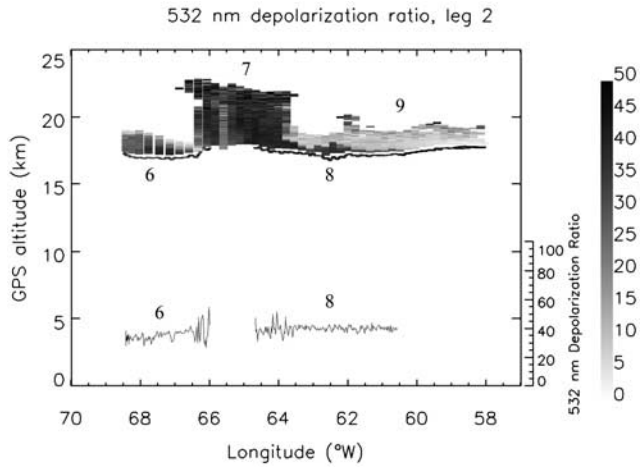

Figure 6. In the upper part, depolarization ratio measured by MAL and MAS. In the lower part the depolarization ratio observed by the backscatter sonde along the flight path is also reported, for clarity. See color version of this figure in the HTML.

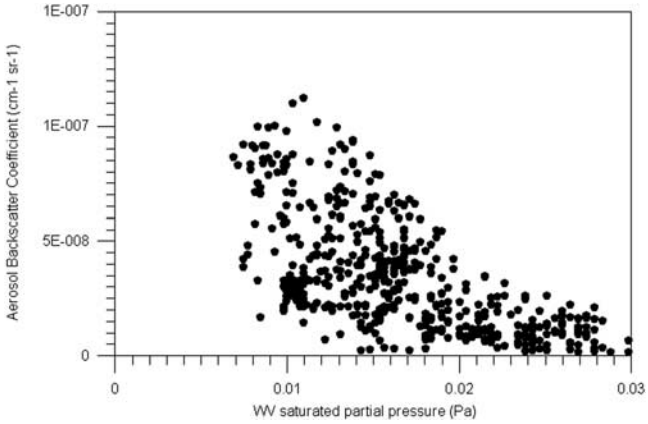

Figure 7. A relationship, grossly linear, between the aerosol backscatter coefficient and the water vapor saturation pressure. The aerosol backscatter coefficient was calculated from the backscattering ratio measured by the backscatter sonde crossing the ice PSC along the flight and contemporary temperature and pressure data from the aircraft avionic sensors. The water vapor saturation pressure was computed making use of the temperature data. A value of total water abundance in the sounded air mass could be inferred from the water vapor saturation value when the aerosol backscattering coefficient is zero.

environmental temperature may lead us to assume that the ice PSC are not exceedingly far from thermodynamical equilibrium. Then we could try to make a gross estimate of the condensed water content of the cloud, or at its least upper and lower limits, by looking at the correlation between the aerosol backscattering coefficient and the saturated water vapor pressure, assuming that the condensation process conserves the water substance in the sounded air mass. Finally, at the onset of condensation, i.e., when aerosol backscattering coefficients are close to zero, the value of the saturated water vapor pressure equals the pressure of all the vapor initially available for condensation. According to this assumption a value around 0.03 Pa is the upper limit of water vapor available for condensation, and values around 0.02 Pa of water vapor were condensed to give the highest backscattering coefficient observed by MAS. These observations have been carried out on a constant pressure level. In this way, the values of water expressed in ppmv turn to be 4.5–5 ppmv of available water vapor and 3 ppmv of water in the condensed phase in the coldest regions, where the thickest PSCs have been observed.

[33] It may be considered atypical to find such amounts of water vapor in the Antarctic stratosphere, at that altitude and time of the year, since a large dehydration has already set up earlier in the season [*Nedoluha et al.*, 2000]. Nevertheless, it has to be taken into account that the PSC observation took place at the boundaries of the vortex, where rehydration from vertical advection or from intrusions of water-rich midlatitude air could have already occurred, rehydrating these air masses.

[34] Lookup tables of aerosol backscattering and depolarization ratio are kindly supplied by B. Luo [*Wirth et al.*, 1999]. These ratios are functions of average particle radius and aspect ratio, computed with the use of T-matrix theory

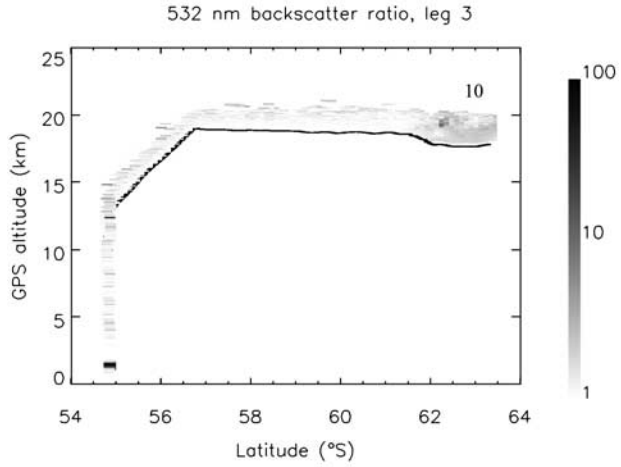

Figure 8. Color-coded backscatter ratio versus altitude-latitude along the third leg of the flight. A wide area of enhanced backscattering, with a more intense spot of backscattering at 19 km altitude, appears at the southernmost point of the leg. See color version of this figure in the HTML.

for aspherical ice particles. Assuming 3 ppmv of condensed water in the cloud, from the tables inspection it is possible to give an estimation of the mean radius of the particles.

[35] The average radius consistent with observations of an aerosol backscatter ratio of 60 and an aerosol depolarization of 30% (mean value) is of the order of 1 μm. This finding is reasonable since the strong and fast cooling rates associated with wave events should lead to formation of particles with high number density and not exceedingly large radii.

[36] Figures 8 and 9 show the backscatter and depolarization ratio, respectively, observed during the third leg.

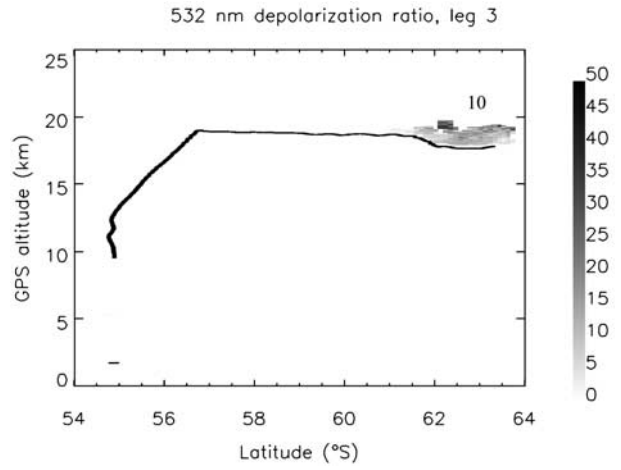

Figure 9. Color-coded depolarization ratio versus altitude-latitude along the third leg of the flight. At the southernmost point of the leg an area of type Ia PSCs, at 19 km altitude, is clearly discernible, with the more intense spot at 19 km altitude being type II. See color version of this figure in the HTML.

Only at the southernmost part of the leg was a PSC observed, with characteristics of type Ia (mark 10).

[37] To summarize, the observations show that PSCs are predominantly of types II and Ia; these latter showing up either upwind or downwind of the ice PSC. Their distribution and pattern with respect to the predicted temperature field over the Palmer Peninsula indicate that they have been caused by mountain wave activity.

4. Microphysical Simulations

4.1. Microphysical and Trajectory Model

[38] Early theories on PSC I and II formation [*Poole and McCormick*, 1988b] considered freezing of the ubiquitous stratospheric layer of submicron-size particles formed by sulfuric acid and water [*Turco et al.*, 1982] to the stable tetrahydrate form of the sulphuric acid (SAT). These frozen aerosol particles then act as condensation nuclei for nitric acid and water to form nitric acid trihydrate (NAT), stable at stratospheric temperatures. So, when the condensation temperature T_{NAT} is reached, a type I cloud is formed. Upon further cooling below T_{ICE}, ice would grow on NAT, forming a fully developed type II ice cloud.

[39] Subsequent theoretical [*Luo et al.*, 1994] and experimental [*Middlebrook et al.*, 1993] studies indicate the unlikeliness of SAT precipitation from binary solution down to temperature below T_{ICE}. Moreover, to explain the existence of liquid type Ib PSC, it has been proposed that the stratospheric sulphate aerosols would remain liquid upon cooling, when they might start to take up HNO_3 and H_2O to form supercooled ternary solutions (STS) [*Carslaw et al.*, 1994] and eventually solidify only below T_{ICE} as water ice, in cases with SAT and NAT particles embedded, or with a liquid or NAT coating [*Peter et al.*, 1994].

[40] In this picture, NAT could nucleate only in ice supersaturated conditions [*Hanson*, 1992], and the formation of type Ia clouds would imply temperatures below T_{ICE} [*Koop et al.*, 1995] in the past history of the air parcel.

[41] Nevertheless, explanations for NAT formation processes above T_{ICE} have also been invoked, such as formation of amorphous solid particles at temperatures above T_{ICE} (type 1c PSC) and subsequent cystallization upon warming [*Tabazadeh and Toon*, 1996]; or direct NAT formation on STS solutions either when strong mesoscale temperature fluctuations lead the droplet composition close to the stoichiometry of NAT [*Meilinger et al.*, 1995; *Song*, 1994] or when temperature dwells long enough inside a well-defined "nucleation window" [*Tabazadeh et al.*, 2001]. There is also a suggestion for heterogeneous freezing in the presence of suitable freezing nuclei [*Drdla et al.*, 2002]. In addition, other metastable forms of nitric acid hydrates, like the dihydrate (NAD), could as well play a role in forming type Ia PSC [*Salcedo et al.*, 2001]. Moreover, the role of SAT in inducing NAT nucleation [*Iraci et al.*, 1994] at temperatures above T_{ICE} is still under debate, since SAT could either deliquesce upon cooling to a temperature some 2–3 degrees above T_{ICE}, or possibly induce a NAT nucleation, depending on the availability of nitric acid in gas phase [*Koop and Carslaw*, 1996]. This latter process could be enhanced if SAT have been previously exposed to the presence of NAT [*Zhang et al.*, 1996].

[42] Field, laboratory and theoretical works resulted in a clear identification of type Ia PSC as formed by solid nitric acid hydrated particles [*Voigt et al.*, 2000b] and type Ib, formed by aqueous solutions of nitric and sulfuric acid [*Schreiner et al.*, 1999]. Nevertheless, the pathways to their formation, as well as the hysteresis effect on their thermal histories, are still a matter of open debate.

[43] The University of L'Aquila aerosol box model has been developed with the aim of providing a tool for the interpretation of PSC observations [*Rizi and Visconti*, 1999]. It has been extensively used in the analysis of data from the MOANA experiment during SESAME [*Rizi et al.*, 1999]. Its structure contains more than 100 subroutines and allows one to update the various processes and thermodynamic data with the newest results. In air masses performing a prescribed isentropic thermal history, the model simulates the evolution of Aitken particles (ATK), H_2O/H_2SO_4 liquid droplets (WS), $H_2O/H_2SO_4/HNO_3$ liquid droplets (WSN), HNO_3 solid hydrates (NA-h), H_2SO_4 solid hydrates (SA-h) and ice particles. The physical processes accounted for in the model are as follows: heteromolecular homogeneous and heterogeneous nucleation of binary WS solution over ATK particles and of NA-h and ice over NA-h and SA-h particles; homogeneous and heterogeneous freezing/melting nucleation of solid NA-h and SA-h from/to WS and WSN liquid solutions; diffusive condensation/evaporation of H_2O, H_2SO_4 and HNO_3 to/from WS and WSN liquid particles and to/from SA-h, NA-h and ice solid particles; coagulation. The model includes the most recent data and results from PSC studies.

[44] The model has been used to simulate possible pathways to PSC formation. Twenty-four hour air parcel thermal histories from ECMWF analysis have been used. The last 3 hours of temperature histories before observations have been also reconstructed with the MM5 model, run in backward mode. Finally, a sensitivity study with respect to the amount of water vapor and HNO_3 available for condensation has been performed.

[45] Four distinct regions of interest (ROI) have been chosen for detailed backward temperature studies. These are framed in boxes in Figures 3 and 5 and identified as ROI A on the first leg, at approximately 65°S along the flight path where no PSC have been detected; ROI B at 67°S on the first leg where the lidar MAL detected a patch of PSC at 23.5 km altitude; ROI C on the second leg, at approximately 65°W which comprehends air parcels where the lidar MAL detected strong PSC events at 20 km of altitude, as well as air parcels close to these but with no PSCs present; ROI D on the second leg along the flight path where the backscatter sonde MAS detected PSCs. On each ROI, a set of points have been chosen to trace back thermal histories, either from ECMWF analysis or integrating the last 3 hours from isentropic mesoscale backtrajectories. Some of the backtrajectories' starting points are marked with open circles in Figures 3 and 5. In order to rule out possible dependence of thermal histories on the particular choice of the points, a chaoticity study has been performed. This study showed how trajectories, originating from points clustered together, remained clustered and experienced similar thermal histories.

[46] The trajectories used to run the microphysical box model are calculated with the global trajectory model of the

University of L'Aquila [*Redaelli*, 1997; *Dragani et al.*, 2002], which was routinely used during the APE campaign as a forecast tool for flight planning [*Redaelli et al.*, 2001]. This is an isentropic model which conserves potential temperature explicitly and makes use of a fourth-order Runge-Kutta time integration scheme to advect particles with a time step of about 20 min. Horizontal components of wind velocity are calculated at particle locations by cubic-spline interpolation from surrounding grid-points. Potential temperature conservation is accomplished by interpolating wind fields on the selected isentropic surface, whose value is obtained from temperature field on pressure levels. Wind, pressure, and temperature fields used to calculate trajectories are taken from the European Centre for Medium-Range Weather Forecasts (ECMWF) operational analyses, available on a regular 1.125° by 1.125° grid over 15 standard pressure levels from 1000 mbar up to 1 mbar, with a temporal resolution of 6 hours. Trajectories can also be calculated using MM5 output meteorological fields, by time-space nesting the MM5 coarse domain in the ECMWF global field used for the calculation, with a time interval of 1 hour. In this latter case, positions and temperatures of the air parcels are calculated and stored every 90 s.

4.2. Trajectories

[47] In Figure 10, three day backward thermal histories for our different ROIs are shown, together with T_{SAT}, (yellow line) T_{NAT} (red line) and T_{ICE} (blue line) computed, along each Lagrangian trajectory, assuming 5 ppmv of water vapor and 10 ppbv of nitric acid. The leftmost panels show reconstructions based on ECMWF while the rightmost panels show the MM5 thermal history reconstructions for the final 3 hours of the trajectories.

[48] On ROIs A and D, points along the flight track allow direct comparison with measured temperatures. There, both synoptic and mesoscale reconstructions are effective in catching the thermal history ending points with the observed temperature values, within 4 K. A common feature of all backtrajectories (all of them remained confined close to the vortex edge) is the presence of a slow temperature oscillation around the SAT melting point in the previous days, followed by a nearly monotonic smooth cooling starting 1 day prior to observations. Differences between synoptic and mesoscale thermal reconstructions are evident in the last 3 hours, where mesoscale reconstructions show oscillations of wider amplitude. For ROI A and even more significantly for ROI B, synoptic temperatures end slightly above T_{ICE}, while mesoscale temperature drops at its level or below. In ROI C, points inside and outside of the PSC regions have been selected for reconstructing thermal histories: In both synoptic and mesoscale reconstructions, points where no PSCs have been observed had their ending temperatures above T_{ICE}. Points where PSC have actually been observed had their ending temperature close to (in the case of synoptic reconstruction) or even below (in the case of mesoscale reconstruction) T_{ICE}. In both reconstructions, temperature oscillates before the trajectory ending point, the mesoscale oscillation being wider, of the order of 15 K, around T_{ICE}. Finally, trajectories for ROI D end around T_{ICE} in both reconstructions.

[49] To summarize, on ROI A both reconstructed thermal histories should allow for PSCs in regions where they actually have not been observed. On ROI B, it is noteworthy that only MM5 mesoscale trajectories allow for ice PSC formation, while ECMWF reconstructions are too warm. On ROI C, although ECMWF reconstructions end around T_{ICE}, only mesoscale backtrajectories have ending temperature below it, thus assuring the formation of ice PSC. Moreover, only the mesoscale reconstructions have marked differences between trajectories with ending points in and out of regions of PSC observations: Only those with ending points within PSC regions reached temperatures significantly below T_{ICE}. Thus, in that region, only mesoscale reconstructions allow for the structure and characteristics of the observed PSC. Finally, on ROI D, both synoptic and mesoscale trajectories allow for PSC formation on all the selected points of interest, with the mesoscale reconstruction showing wider oscillations.

[50] Our subsequent studies have been concentrated on ROI C, where detailed microphysical models have been run to reconstruct PSC formation. We used the mesoscale reconstruction of the thermal histories, which seemed to better match the observed PSC structure.

4.3. PSC Formation Simulations

[51] We have performed simulations of PSC formation in points at 20 km height, in ROI C. Three regions of study have been defined: region 1, upwind of the type II PSC region where no PSCs where detected by MAL; region 2, inside the type II PSC region; region 3, downwind of the ice clouds, where a large region of type Ia PSCs was detected in their wake. Three scenarios for PSC formation have been investigated. The first one is the SNI scenario: NAT nucleating on SAT above the frost point, then forming ice below the frost point. The second one is the WNS scenario: liquid background aerosol growing to STS, and eventually to ice, the latter leaving NAT upon evaporation. In some simulations we used a third scenario, WNS-special, where we tested the formation of NAT from STS at temperatures above the frost point. For this purpose, we apply the following special nucleation criterion: When the weight fraction of HNO_3 in STS droplets reached the stoichometric ratio close to NAT (triggered by fast warming-cooling cycles), 50% of those droplets were allowed to condense to form NAT.

[52] In all simulated scenarios, points upwind of the ice towers in region 1 did not produce PSCs, while they do form ice PSC in region 2, where they have actually been observed. In this region the final size distributions of the ice particles produced by the SNI pathway of PSC formations were quite insensitive to the amount of HNO_3 available for condensation, which we varied from 10 to 7 to 5 ppbv, and the final size distributions achieved a modal radius around 2 μm. On the contrary, the WNS-special scenario, allowing for NAT formation above T_{ICE}, creates final size distributions that are heavily dependent on the available HNO_3 in gas phase, shifting the modal radius to greater values as this availability decreased: Only when the nitric acid abundance was above 7 ppbv was the modal radius of the size distribution close to 1 μm. In the WNS scenario, where the NAT formation above T_{ICE} was inhibited, the final size distributions of ice particles were much less sensitive to the amount of nitric acid in the gas phase and quite similar to the ones developed in the SNI scenario.

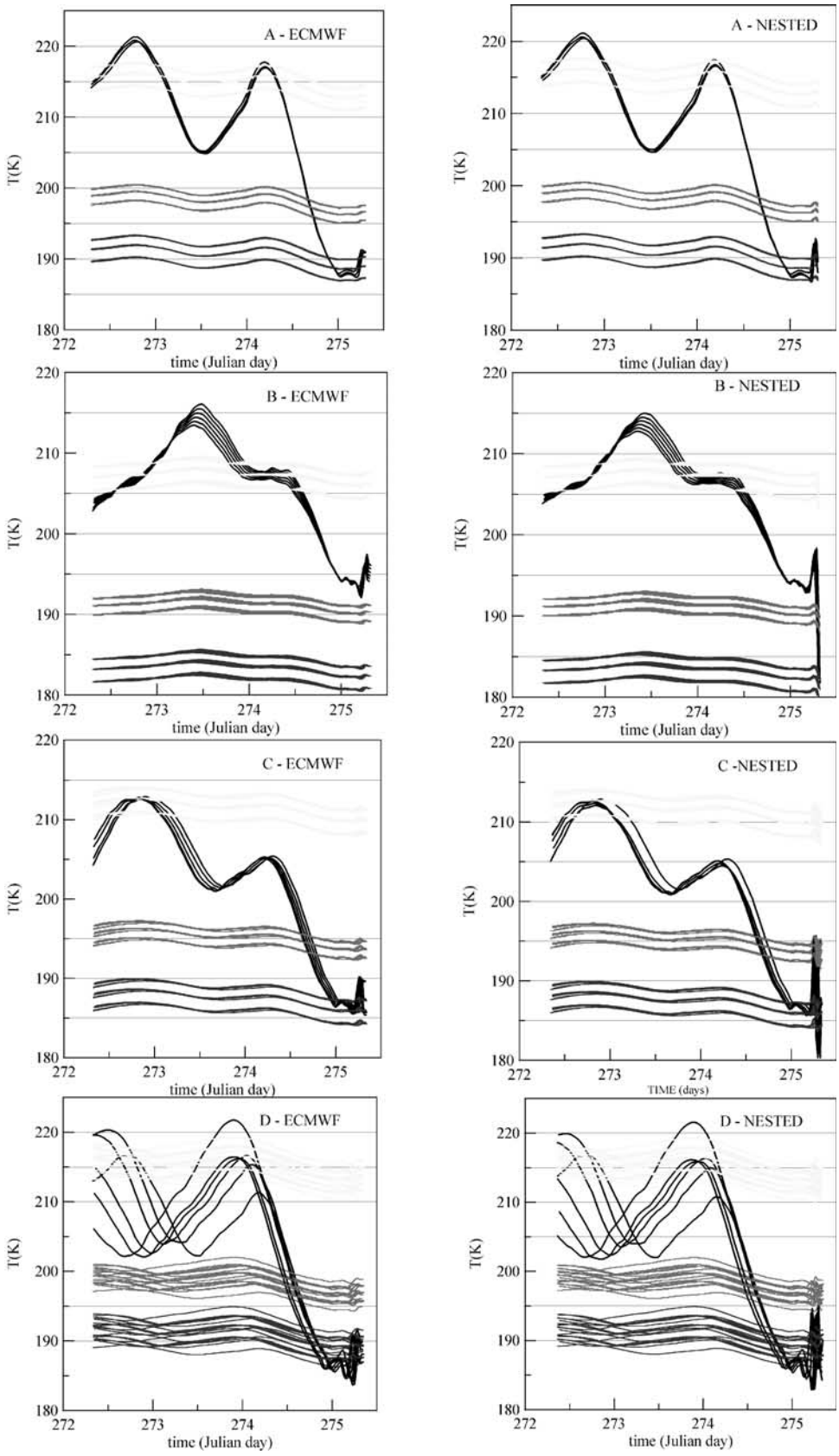
A - ECMWF
A - NESTED
B - ECMWF
B - NESTED
C - ECMWF
C -NESTED
D - ECMWF
D - NESTED
T(K)
time (Julian day)
TIME (days)
180
190
200
210
220
272
273
274
275

Figure 10.

Table 1. Outcomes of Different PSC Formation Scenarios

	SNI Scenario: NAT Nucleating on Preexisting SAT	WNS Scenario: Background Aerosol Growing to STS, Then to Ice, Leaving NAT and/or STS Upon Warming	WNS-Special Scenario: Background Aerosol Growing to STS and/or NAT, Then to Ice, Leaving NAT and/or STS Upon Warming
Region 1	no PSC forming, in accordance with observations	no PSC forming, in accordance with observations	no PSC forming, in accordance with observations
Region 2	ice PSC forming, in accordance with observations	ice PSC forming, in accordance with observations	ice PSC forming, but only when HNO_3 was above 7 ppbv, their optical properties in accordance with observations
Region 3	NAT PSC forming, in accordance with observations	only STS PSC forming, if HNO_3 below 10 ppbv, not in accordance with observations; if HNO_3 at 10 ppbv, STS and NAT PSC forming, but depolarization too low compared to the observed	STS and NAT PSC forming, if HNO_3 below 7 ppbv, not in accordance with observed depolarization; NAT PSC dominated if HNO_3 above 7 ppbv, in accordance with observed depolarization

[53] Unfortunately, our observations, lacking size-resolving particle measurements, are inadequate to properly constrain the results of these modeled scenarios, and no preferred pathway could be discerned in this case.

[54] More dissimilar outputs for the different pathways have been found where the type Ia PSCs were observed: in region 3, in the wake of the two-tower pattern of ice PSCs. There, in the WSN scenario, holding fixed at 5 ppmv the water vapor amount, it was only with the highest amount of HNO_3 that the simulation was able to form a mixed phase PSC. This mixed PSC was composed of ice, STS and NAT. In this case, the STS part of the size distribution prevailed, and ice was quickly evaporating, while the contribution of NAT to the total surface of the particle remained below 20% of the total. If the amount of HNO_3 in gas phase was reduced from 10 ppbv to 7 ppbm, only STS was formed, with no contribution at all from NAT. So this scenario was very sensitive to the amount of HNO_3 in the gas phase: Only when this amount was large was the model able to form NAT. Nevertheless, the produced NAT was not enough to meet the depolarization values observed in that region. To a lesser extent, a dependence on available water vapor was also found: A decrease to 3 ppmv robustly increased the amount of STS in the final state of the mixed cloud. This scenario was the least effective in matching the observations in region 3.

[55] In the WNS-special scenario, mixed phase PSC of STS and NAT were always formed irrespective of the water and nitric acid abundance. A quantitative accordance with the observed optical parameters was obtained only when the nitric acid availability was increased to 10 ppbv, since only then NAT dominated the particle population.

[56] The SNI scenario was always able to form NAT in the wake of the type II PSC, in qualitative agreement with the observations. Since in these scenarios the NAT surface increased almost linearly with increased availability of HNO_3 in gas phase, it was only with the higher abundances of nitric acid that a quantitative agreement with the observations was obtained.

[57] To summarize, although the observations fail to fully constrain the modeling to a single preferred pathway of PSC formation, all the model results suggest an abundance of nitric acid between 7 and 10 ppmv. As previously noted for water vapor abundances, this may be regarded as unusual in the Antarctic vortex in late October, but as already pointed out, it has to be stressed that these observations took place in a boundary region of the vortex, where partial renitrification from midlatitude intrusions could have already occurred. Table 1 summarizes the results of our investigation.

5. Conclusions

[58] Observations, characteristics and locations of PSC on 2 October correlate well with the temperature field as forecasted 36 hours in advance by the MM5 model. All these PSCs were composed of solid particles, either ice or NAT above the ice frost point. Although detailed microphysical measurements on particle size distribution are lacking, indirect evidence on the average dimension of the particles, based on estimations of the condensed mass and comparison of measured optical parameters with optical modeling, indicates the predominance of particles with 1 μm average radius where the ice PSCs were observed. The presence of particles with an average radius around 1 μm in the ice PSC region is further supported by results from microphysical modeling. The modeling often produced a size distribution with modal radius close to our estimates, when the highest amounts of water and nitric acid in the gas phase were made available to condense.

[59] The observed PSC are in a sense ''synoptics'' in their spatial extension. Nevertheless, the microphysical modeling clearly shows how the ice PSCs may not result from

Figure 10. Plots of air temperature versus Julian day for 3 day backward thermal histories, together with T_{SAT}, T_{NAT} and T_{ICE} calculated 10 ppbv of nitric acid and for 5 ppmv of water vapor. Four different regions of interest (ROIs A, B, C and D), corresponding to the areas framed in boxes in Figures 3 and 5, are shown in the first, second, third and fourth rows of the figure, respectively. For each ROI, representative trajectories are depicted. Ending points of trajectories correspond to the points marked with open circles in Figures 3 and 5. The leftmost column shows thermal histories reconstructed from ECMWF temperature fields. The rightmost column shows the MM5 reconstructed temperatures at the end of the thermal histories, 3 hours before the observations. See color version of this figure in the HTML.

synoptic cold temperature fields, but rather originated from the peculiar mesoscale condition dominated by the intense wave activity. However, the observations were consistent with many of the possible pathways leading to PSC formation that we tested in our microphysical model. The lack of any constraint on the availability of water and nitric acid in the vapor phase and size-resolved particle detections does not indicate a preferred pathway among the feasible options.

[60] **Acknowledgments.** We acknowledge the support of Programma Nazionale di Ricerche in Antartide (PNRA), Italy, which funded most of the aircraft preparation and campaign activities. We thank Agenzia Spaziale Italiana (ASI), Italy, Consiglio Nazionale delle Ricerche (CNR), Italy, Parco Scientifico e Tecnologico d'Abruzzo (PSTdA), Italy, Bundesministerium für Bildung, Wissenschaft, Forschung and Tecnologie (BMBF), Germany, Natural Environment Research Council (NERC), UK, Royal Society, UK, OFES and FNRS, Switzerland, European Science Foundation (ESF), and European Union (EU), which concurred in supporting the campaign.

References

Adriani, A., F. Cairo, M. Viterbini, S. Mandolini, L. Pulvirenti, and G. Di Donfrancesco (1999), Multiwavelength aerosol scatterometer for airborne experiments to study the optical properties of stratospheric aerosol, *J. Atmos. Oceanic Technol.*, *16*, 1328–1335.

Behrendt, A., and T. Nakamura (2002), Calculation of the calibration constant of polarization lidar and its dependency on atmospheric temperature, *Opt. Express*, *10*, 805–817.

Browell, E. V., C. F. Butler, S. Ismail, P. A. Robinette, A. F. Carter, N. S. Higdon, O. B. Toon, M. R. Schoeberl, and A. F. Tuck (1990), Airborne lidar observations in the wintertime Arctic stratosphere: Polar stratospheric clouds, *Geophys. Res. Lett.*, *17*, 385–388.

Cairo, F., et al. (2000a), A large event of polar stratospheric cloud observed over the Antarctic Peninsula with the airborne laser backscattersonde MAS and the lidar MAL, in comparison with synoptic and mesoscale modeling, in *Proceedings of the Quadriennal Ozone Symposium: Sapporo 2000*, pp. 327–328, Natl. Space Dev. Agency of Japan, Tsukuba.

Cairo, F., et al. (2000b) Presence of a stratospheric thin laminar structure of aerosol observed by backscattersonde MAS and the lidar MAL in the APE-GAIA campaign, in *Proceedings of the Quadriennal Ozone Symposium: Sapporo 2000*, pp. 329–330, Natl. Space Dev. Agency of Japan, Tsukuba.

Carli, B., U. Cortesi, C. E. Blom, M. P. Chipperfield, G. De Rossi, and G. Redaelli (2000), Airborne Polar Experiment Geophysica Aircraft in Antartica (APE-GAIA), *SPARC Newsl.*, *15*, 21–24.

Carslaw, K. S., B. Luo, S. L. Clegg, T. Peter, P. Briblecombe, and P. J. Crutzen (1994), Stratospheric aerosol growth and HNO_3 gas phase depletion from coupled HNO_3 and water uptake by liquid particles, *Geophys. Res. Lett.*, *21*, 2479–2482.

di Sarra, A., M. Cacciani, G. Fiocco, D. Fuà, and T. S. Jørgensen (2002), Lidar observations of polar stratospheric clouds over northern Greenland in the period 1990–1997, *J. Geophys. Res.*, *107*(D12), 4152, doi:10.1029/2001JD001074.

Dörnbrack, A., T. Birner, A. Fix, H. Flentje, A. Meister, H. Schmid, E. V. Browell, and M. J. Mahoney (2002), Evidence for inertia gravity waves forming polar stratospheric clouds over Scandinavia, *J. Geophys. Res.*, *107*(D20), 8287, doi:10.1029/2001JD000452.

Dragani, R., G. Redaelli, A. Mariotti, V. V. Rudakov, A. R. MacKenzie, L. Stefanutti, and G. Visconti (2002), High resolution stratospheric tracer fields reconstructed with Lagrangian techniques: A comparative analysis of predictive skill, *J. Atmos. Sci.*, *59*, 1943–1958.

Drdla, K., M. R. Schoeberl, and E. V. Browell (2002), Microphysical modeling of the 1999–2000 Arctic winter: 1. Polar stratospheric clouds, denitrification, and dehydration, *J. Geophys. Res.*, *107*, 8312, doi:10.1029/2001JD000782. [printed *108*(D5), 2003]

Ferretti, R., T. Paolucci, W. Zheng, G. Visconti, and G. Bonelli (2000), Analyses of the precipitation pattern on the Alpine region using different cumulus convection parametrizations, *J. Appl. Meteorol.*, *39*, 182–200.

Fiocco, G., P. Calisse, M. Cacciani, S. Casadio, G. Pace, and D. Fuà (1999), ABLE: Development of an airborne lidar, *J. Atmos. Oceanic Technol.*, *16*, 1337–1344.

Fromm, M. D., J. D. Lumpe, R. M. Bevilacqua, E. P. Shettle, J. Hornstein, S. T. Massie, and K. H. Fricke (1997), Observations of Antarctic polar stratospheric clouds by POAM II: 1994–1996, *J. Geophys. Res.*, *102*, 23,659–23,672.

Hanson, D. R. (1992), The uptake of HNO3 onto ice, NAT, and frozen sulfuric acid, *Geophys. Res. Lett.*, *19*, 2063–2066.

Hanson, D., and K. Mauersberger (1988), Laboratory studies of the nitric acid trihydrate: Implication for the south polar stratosphere, *Geophys. Res. Lett.*, *15*, 855–858.

Iraci, L. T., A. M. Middlebrook, M. A. Wilson, and M. A. Tolbert (1994), Growth of nitric acid hydrates on thin sulphuric acid films, *Geophys. Res. Lett.*, *21*, 867–870.

Koop, T., and K. S. Carslaw (1996), Melting of H_2SO_4*$4H_2O$ particles upon cooling: Implications for polar stratospheric clouds, *Science*, *272*, 1638–1641.

Koop, T., U. P. Bieermann, W. Raben, B. Luo, P. J. Crutzen, and T. Peter (1995), Do stratospheric aerosol freeze above the ice frost point?, *Geophys. Res. Lett.*, *22*, 917–920.

Luo, B., T. Peter, and P. Crutzen (1994), Freezing of stratospheric droplets, *Geophys. Res. Lett.*, *21*, 1447–1450.

Marti, J., and K. Mauersberger (1993), A survey and new measurements of ice vapor pressure at temperatures between 170 and 250 K, *Geophys. Res. Lett.*, *20*, 363–366.

Matthey, R., V. Mitev, G. Mileti, A. Makarov, A. Turin, M. Morandi, and V. Santacesarea (2000), Miniature aerosol lidar for automated airborne application, in *Laser Radar Technology and Application V*, edited by G. V. Kamerman et al., *Proc. SPIE Int. Soc. Opt. Eng.*, *4035*, 44–53.

Meilinger, S. K., T. Koop, B. Luo, T. Huthwelker, and K. Carslaw (1995), Size-dependent stratospheric droplet composition in lee wave temperature fluctuations and their potential role in PSC freezing, *Geophys. Res. Lett.*, *22*, 3031–3034.

Middlebrook, A. M., L. T. Iraci, L. S. McNeill, B. G. Koehler, M. A. Wilson, O. W. Saastad, M. A. Tolbert, and D. R. Hanson (1993), Fourier transform infrared studies of thin H_2SO_4/H_2O films: Formation, water uptake and solid-liquid phase changes, *J. Geophys. Res.*, *98*, 20,473–20,481.

Nedoluha, G. E., R. M. Bevilacqua, K. W. Hoppel, M. Daehler, E. P. Shettle, J. H. Hornstein, M. D. Fromm, J. D. Lumpe, and J. E. Rosenfield (2000), POAM III measurements of dehydration in the Antarctic lower stratosphere, *Geophys. Res. Lett*, *27*, 1683–1686.

Peter, T., R. Muller, and P. J. Crutzen (1994), The lifetime of lee-wave induced ice particles in the Arctic stratosphere: II. Stabilization due to NAT coating, *Geophys. Res. Lett.*, *21*, 1331–1334.

Poole, L. R., and M. P. McCormick (1988a), Airborne lidar observations of Arctic polar stratospheric clouds: Indications of two distinct growth stages, *Geophys. Res. Lett.*, *15*, 21–23.

Poole, L. R., and M. P. McCormick (1988b), Polar stratospheric clouds and the Antarctic ozone hole, *J. Geophys. Res.*, *93*, 8423–8430.

Poole, L. R., and M. C. Pitts (1994), Polar stratospheric cloud climatology based on Stratospheric Aerosol Measurement II observations from 1978 to 1989, *J. Geophys. Res.*, *99*, 13,083–13,089.

Poole, L. R., S. Solomon, M. P. McCormick, and M. C. Pitts (1989), The interannual variability of polar stratospheric clouds and related parameters in Antartica during September and October, *Geophys. Res. Lett.*, *16*, 1157–1160.

Redaelli, G. (1997), Tecniche Lagrangiane per l'analisi di misure in stratosfera, Ph.D. dissertation, Univ. of L'Aquila, L'Aquila, Italy.

Redaelli, G., R. Dragani, B. Grassi, V. V. Rudakov, A. Ulanovsky, C. M. Volk, O. Riediger, F. Ravegnani, and G. Visconti (2001), Model guided observation and simulation of vortex filament during APE/GAIA, paper presented at XXVI European Geophysical Society General Assembly, Nice, France, April.

Rizi, V., and G. Visconti (1999), Physical analogs and performance of a box model for composition and growth of H_2SO_4/H_2O and $HNO_3/H_2SO_4/H_2O$ aerosol in the stratosphere, *J. Aerosol Sci.*, *30*, 1095–1113.

Rizi, V., et al. (1999), Trajectory studies of polar stratospheric cloud lidar observations at Sodankyla (Finland) during SESAME: Comparison with box model results of particle evolution, *J. Atmos. Chem.*, *32*, 165–181.

Salcedo, D., L. T. Molina, and M. J. Molina (2001), Homogeneous freezing of concentrated aqueous nitric acid solutions at polar stratospheric temperatures, *J. Phys. Chem. A*, *105*, 1433–1439.

Santacesarea, V., M. Morandi, L. Stefanutti, V. Mitev, R. Matthey, V. Makarov, A. Adriani, F. Cairo, and G. Di Donfrancesco (2000), Microjoule lidar observations of aerosol and cloud during the APE-THESEO mission around the tropical tropopause, *Stratospheric Ozone 1999: Proceedings of the Fifth European Symposium*, *Eur. Comm. Air Pollut. Res. Rep. 73*, edited by N. R. P. Harris, M. Guirlet, and G. T. Amanatidis, pp. 653–656, Eur. Comm., Brussels.

Schreiner, J., C. Voigt, K. Mauersberger, F. Arnold, and N. Larsen (1999), Chemical analysis of polar stratospheric cloud particles, *Science*, *283*, 968–970.

Solomon, S. (1999), Stratospheric ozone depletion: A review of concept and history, *Rev. Geophys.*, *37*, 275–316.

Song, N. (1994), Freezing temperatures of $H_2SO_4/HNO_3/H_2O$ mixtures: Implications for polar stratospheric clouds, *Geophys. Res. Lett.*, *21*, 2709–2712.

Stannford, J. L., and J. S. Davis (1974), A century of stratospheric clouds reports: 1870–1972, *Bull. Am. Meteorol. Soc.*, *55*, 213–219.

Tabazadeh, A., and O. B. Toon (1996), The presence of metastable HNO_3/H_2O solid phases in the stratosphere inferred from ER-2 data, *J. Geophys. Res.*, *101*, 9071–9078.

Tabazadeh, A., E. J. Jensen, O. B. Toon, K. Drdla, and M. R. Schoeberl (2001), Role of the stratospheric polar freezing belt in denitrification, *Science*, *291*, 2591–2594.

Tsias, A., et al. (1999), Aircraft lidar observations of an enhanced type 1a polar stratospheric clouds during APE-POLECAT, *J. Geophys. Res.*, *104*, 23,961–23,969.

Turco, R. P., R. C. Whitten, and O. B. Toon (1982), Stratospheric aerosols: Observation and theory, *Rev. Geophys.*, *20*, 233–279.

Voigt, C., A. Tsias, A. Dörnbrack, S. Meilinger, B. Luo, J. Schreiner, N. Larsen, K. Mauersberger, and T. Peter (2000a), Non-equilibrium compositions of liquid polar stratospheric clouds in gravity waves, *Geophys. Res. Lett.*, *27*, 3873–3876.

Voigt, C., et al. (2000b), Nitric acid trihydrate (NAT) in polar stratospheric clouds, *Science*, *290*, 1756–1758.

Wirth, M., A. Tsias, A. Dörnbrack, V. Weiss, K. S. Carslaw, M. Leutbecher, W. Renger, H. Volkert, and T. Peter (1999), Model-guided Lagrangian observation and simulation of mountain polar stratospheric clouds, *J. Geophys. Res.*, *104*, 23,971–23,981.

Young, A. T. (1980), Rayleigh scattering, *Appl. Opt*, *20*, 533–535.

Zhang, R. Y., M. T. Leu, and M. J. Molina (1996), Formation of polar stratospheric clouds on preactivated background aerosols, *Geophys. Res. Lett.*, *23*, 5215–5227.

A. Adriani, IFSI, Area di Ricerca di Tor Vergata, Via Fosso del Cavaliere 100, I-00133 Roma, Italy. (adriani@atmos.ifa.rm.cnr.it)

M. Bastiano and G. Pace, ENEA C.R. Casaccia, Via Anguillarese 301, I-00060 Santa Maria di Galeria (Roma), Italy. (maurizio.bastiano@ne.ch; pace@g24ux.phys.uniroma1.it)

L. Bernardini and T. Paolucci, Dipartimento di Fisica/INFN/PSTd'A-Gruppo Collegato dell'Aquila, Via Vetoio Località Coppito, I-67100 L'Aquila, Italy. (livio.bernardini@aquila.infn.it; tiziana.paolucci@aquila.infn.it)

M. Cacciani and G. Fiocco, Dipartimento di Fisica, Università degli studi di Roma "La Sapienza," Piazzale Aldo Moro 2, I-00185 Roma, Italy. (cacciani@g24ux.phys.uniroma1.it; fiocco@g24ux.sci.uniromal.it)

F. Cairo and M. Viterbini, Istituto di Scienze dell'Atmosfera e del Clima, CNR, Via Fosso del Cavaliere 100, I-00133 Roma, Italy. (f.cairo@isac.cnr.it; m.viterbini@isac.cnr.it)

G. Di Donfrancesco, ENEA C.R. Frascati, Via Enrico Fermi 45, I-00044 Frascati (Roma), Italy. (didonfrancesco@frascati.enea.it)

R. Dragani, R. Ferretti, G. Redaelli, and V. Rizi, Dipartimento di Fisica, Università degli Studi dell'Aquila, Via Vetoio, Localita Coppito, I-67010 L'Aquila, Italy. (rossana.dragani@aquila.infn.it; rossella.ferretti@aquila.infn.it; redaelli@aquila.infn.it; vincenzo.rizi@aquila.infn.it)

R. Matthey and V. Mitev, Observatoire Cantonal de Neuchâtel, Rue de l'Observatoire 68, CH-2000 Neuchâtel, Switzerland. (renaud.matthey@ne.ch; valentin.mitev@ne.ch)